nature physics

ARTICLES

https://doi.org/10.1038/s41567-019-0516-6

Stress relaxation in epithelial monolayers is controlled by the actomyosin cortex

Nargess Khalilgharibi[1,2], Jonathan Fouchard[1], Nina Asadipour[3], Ricardo Barrientos[2,4], Maria Duda[4], Alessandra Bonfanti[5], Amina Yonis[1,6], Andrew Harris[1,7,8,9], Payman Mosaffa[3], Yasuyuki Fujita[10], Alexandre Kabla[5], Yanlan Mao[4], Buzz Baum[4,11], José J Muñoz[3,12], Mark Miodownik[13] and Guillaume Charras[1,6,11]*

Epithelial monolayers are one-cell-thick tissue sheets that line most of the body surfaces, separating internal and external environments. As part of their function, they must withstand extrinsic mechanical stresses applied at high strain rates. However, little is known about how monolayers respond to mechanical deformations. Here, by subjecting suspended epithelial monolayers to stretch, we find that they dissipate stresses on a minute timescale and that relaxation can be described by a power law with an exponential cut-off at timescales larger than about 10 s. This process involves an increase in monolayer length, pointing to active remodelling of cellular biopolymers at the molecular scale during relaxation. Strikingly, monolayers consisting of tens of thousands of cells relax stress with similar dynamics to single rounded cells, and both respond similarly to perturbations of the actomyosin cytoskeleton. By contrast, cell–cell junctional complexes and intermediate filaments do not relax tissue stress, but form stable connections between cells, allowing monolayers to behave rheologically as single cells. Taken together, our data show that actomyosin dynamics governs the rheological properties of epithelial monolayers, dissipating applied stresses and enabling changes in monolayer length.

Epithelial monolayers line most surfaces and internal cavities of the body, acting as physical barriers between the internal and the external environment. For this, epithelia must withstand substantial mechanical stresses[1–4]. During development, strain in epithelia evolves slowly at rates of about 0.04% s^{-1} (ref. [5]); in adult animals, strain rates of 10–100% s^{-1} occur during normal organ function[6–10]. While in some organs, such as the lung, epithelia are subjected to deformations lasting only seconds, in others (skin, intestine, bladder) large deformations can be sustained for minutes[10–12]. In addition, organisms need to withstand external mechanical insults. Thus, for optimal tissue resilience, the cells must be mechanically integrated to spread stresses across the whole tissue. Failure to do so can result in tissue fracture with consequences such as haemorrhage and septicaemia[13–15]. Indeed, tissue fragility appears as a symptom in patients carrying mutations in intermediate filaments and desmosomal proteins[16], adherens junction proteins and actin cytoskeletal regulators[17,18], and because of bacterial pathogens targeting intercellular adhesions[16]. The ability of living tissues to dissipate stresses decreases the risk of fracture[19], protecting organisms against failure. Despite the importance of epithelial mechanics, little is known about how epithelia dissipate stresses in response to extension.

In isolated cells, many rheological behaviours operating at different timescales have been identified. At subsecond timescales, localized stress applied to the cell surface can be dissipated by redistribution of the fluid phase cytosol through the porous insoluble part of the cytoplasm[20]. At longer timescales, a scale-free power law rheology is observed[20,21], and recent work has indicated the presence of a cut-off to this response imposed by the actomyosin cytoskeleton[22]. In multicellular aggregates, rheology may be influenced by the assembly of specialized intercellular junctions and junctional signalling[23,24]. Indeed, adherens junctions, which link the actin cytoskeletons of adjacent cells, exhibit viscoelastic properties[25]. However, little is known about the stress response of cultured or embryonic epithelia to deformation—despite this being an important property for tissues. Nor is it known which molecular mechanisms participate in the process. In part, this derives from the difficulty of measuring stress in epithelia mechanically coupled to a relatively thick and rigid extracellular matrix (ECM).

Here, we study stress relaxation in epithelial monolayers devoid of ECM subjected to a physiologically relevant strain. Our analysis reveals that, at minute timescales, tissue rheology is dominated by the actomyosin cytoskeleton and that myosin contractility accelerates stress relaxation. By contrast, adherens junctions act as stable bridges connecting adjacent cells. As a consequence, the stress relaxation of an epithelial monolayer is similar to that of an isolated cell.

Stress relaxation is accompanied by a change in length

To investigate the response of epithelia to stress, we used monolayers of Madin–Darby Canine Kidney (MDCK II) cells devoid of a

[1]London Centre for Nanotechnology, University College London, London, UK. [2]Centre for Computation, Mathematics and Physics in the Life Sciences and Experimental Biology (CoMPLEX), University College London, London, UK. [3]Laboratori de Càlcul Numèric (LaCàN), Department of Mathematics, Escola d'Enginyeria Barcelona Est (EEBE), Universitat Politècnica de Catalunya—Barcelona Tech (UPC), Barcelona, Spain. [4]MRC Laboratory for Molecular Cell Biology, University College London, London, UK. [5]Department of Engineering, Cambridge University, Cambridge, UK. [6]Department of Cell and Developmental Biology, University College London, London, UK. [7]Department of Physics, University College London, London, UK. [8]Engineering Doctorate Program, Department of Chemistry, University College London, London, UK. [9]Department of Bioengineering and Biophysics Program, University of California, Berkeley, Berkeley, CA, USA. [10]Institute for Genetic Medicine, Hokkaido University, Hokkaido, Japan. [11]Institute for the Physics of Living Systems, University College London, London, UK. [12]Barcelona Graduate School of Mathematics (BGSMath), Barcelona, Spain. [13]Department of Mechanical Engineering, University College London, London, UK. *e-mail: g.charras@ucl.ac.uk

substrate and suspended between test rods[13,26]. Under these conditions, all stress in the system is borne by cells, simplifying interpretation and analysis (Supplementary Fig. 1). Suspended monolayers were subjected to a strain $\varepsilon_0 = 30\%$ applied at a rate of $75\%\,s^{-1}$, within the linear regime of the stress–strain response for monolayers[13] and consistent with in vivo physiological conditions[7,10,27]. Strain was then maintained for about 130–140 s (Fig. 1a,b and Methods), while stress was monitored. Strikingly, about 70% of stress was dissipated within about 60 s (Fig. 1c). Importantly, this behaviour was reproducible over several cycles. Moreover, cells maintained their characteristic apico-basal polarity and cytoskeletal organization throughout[13,28]. In the body, epithelia are generally bound to ECM. Therefore, we confirmed the generality of the observed stress relaxation behaviour in a simple tissue comprising cells and ECM using *Drosophila* third larval instar wing imaginal discs (Fig. 1d,e and Supplementary Results). Wing discs displayed behaviours qualitatively similar to those of monolayers, although the amplitude of stress relaxation was lower, probably because of the presence of ECM.

In living tissues, stress relaxation can arise from molecular or cellular processes. In our experiments, cellular processes, such as oriented cell division or neighbour exchange[1,19,29], are unlikely to contribute, since they require tens of minutes (Fig. 1c,f). During stress relaxation, we could not observe any changes in organization or cell morphology (Supplementary Fig. 2c,d and Supplementary Results). Nevertheless, when the test rod is returned to its initial position at the end of an experiment, the monolayer buckles (Fig. 1g and Supplementary Video 1). Thus, stress relaxation involves an increase in monolayer length as a result of remodelling at the subcellular scale.

Monolayer stress relaxation is biphasic

Stress relaxation started immediately after extension and was biphasic, with a large-amplitude fast relaxation occurring within the first approximately 6 s, followed by a smaller-amplitude slow relaxation, which reached a plateau after about 60 s, as previously observed[13] (Figs. 1c and 2a). This plateau indicates that the material behaves like a solid at minute timescales. Examination of the relaxation curves in log–log and log–linear scales revealed that stress decays as a power law in the first phase and as an exponential in the second (Supplementary Fig. 3). We confirmed the power-law nature of the first phase by performing stress relaxation experiments for a range of deformations (Supplementary Fig. 4c–f and Supplementary Methods). Based on these observations, the relaxation can be described by $At^{-\alpha}e^{-t/\tau}+B$ (Methods), with the first phase characterized by the exponent α and the second phase by the time constant τ ($\alpha = 0.3 \pm 0.03$, $\tau = 14.9 \pm 5.8$ s, $n = 17$ monolayers). B/ε_0 is equivalent to an elasticity, and A sets the amplitude of the relaxation. Interestingly, the power-law exponent $\alpha \sim 0.30$ was consistent with reports for cell aggregates subjected to compression[30]. Relaxation in *Drosophila* wing discs displayed similar characteristics, although the parameters differed (Supplementary Fig. 5c–h, Supplementary Table 2 and Supplementary Results). Thus, larval and cultured epithelia display fluid-like properties at second timescales and solid-like properties at minute timescales.

To explore the robustness of this biphasic behaviour, we subjected cultured monolayers to a 30% strain applied at different rates and to different strains at a fixed $75\%\,s^{-1}$ rate. In both cases, the data were well described by our empirical fit function (Supplementary Figs. 6 and 8 and Supplementary Results). Taking loading into account, we confirmed that our initial experimental conditions (30% strain applied at $75\%\,s^{-1}$) are close to a pure step strain for monolayers, validating our fitting approach (Supplementary Figs. 6 and 7 and Supplementary Results). Interestingly, τ increased with strain with a slope significantly larger than zero (Supplementary Fig. 8g, slope $= 70.1 \pm 57.1$ s, $P < 0.05$). The dependence of τ on strain is surprising and may arise because the rate of processes dissipating stress does not depend on strain.

The transition between the two relaxation phases occurs for $t \sim 6$ s (Supplementary Fig. 3c). This short timescale suggests that passive, ATP-independent processes govern the power-law behaviour, while active ATP-dependent processes participate in the second phase. When we examined stress relaxation curves from ATP-depleted tissues on a log–log scale, we noticed that they did not display the plateau at long timescales characteristic of exponential relaxation (Fig. 2a–c, Supplementary Fig. 4a and Supplementary Results), indicating that the second phase was indeed ATP dependent.

Monolayer stress relaxation depends on actomyosin

As stress relaxation is accompanied by an increase in monolayer length, we hypothesized that it may involve dynamic turnover of cytoskeletal and adhesive structures. We focused on subcellular structures known to play a role in cell and tissue mechanics[31,32], such as the actin cytoskeleton[13,33–35], intermediate filaments[36,37] and the intercellular junctions connecting these structures (adherens junctions[13,38,39] and desmosomes[15]).

To identify key components of these structures in MDCK monolayers, we used messenger RNA sequencing (Supplementary Methods), and selected proteins that were among the most abundant in each candidate structure for further examination (Supplementary Fig. 9a).

We reasoned that only proteins that display extensive turnover on the timescale of our experiments could significantly contribute to stress relaxation. To characterize turnover, we used fluorescence recovery after photobleaching (FRAP) and estimated the extent of recovery after 100 s (mobile fraction, Supplementary Methods, Fig. 2e,f, Supplementary Fig. 9b,c and Supplementary Table 1). Actin, myosin and crosslinkers were the most dynamic, with mobile fractions larger than 0.4, consistent with a potential role in stress relaxation (Fig. 2f and Supplementary Table 1). In contrast, proteins of the cadherin–catenin complex, intermediate filaments and desmosomes seemed stable, with mobile fractions smaller than 0.1. Proteins involved in mechanotransduction exhibited intermediate mobility (EPLIN and vinculin).

To test for a role for actomyosin, we depolymerized F-actin using latrunculin B (Fig. 3a,b). This led to a remarkable softening of the monolayer, suggesting that intermediate filaments bear little stress in this range of strain (Fig. 3c,d). Furthermore, relaxation curves appeared linear in the logarithmic scale, pointing to a delay in the second phase or its abrogation (Fig. 3d). Thus, the actin cytoskeleton governs the second phase of relaxation. As actin-related proteins with fast turnover localized to both intercellular junctions and the submembranous cortex (Supplementary Fig. 10), this suggested that either of these actomyosin-rich structures may contribute to relaxation in the second phase.

Perturbing actomyosin slows relaxation

Actin's function is multifaceted: it is the building block for generating filamentous actin, F-actin serves as a scaffold for myosin contractility, and crosslinkers can modulate the network's mechanics.

Previous work has identified specific roles for actin networks generated through distinct nucleation pathways via the Arp2/3 complex and formins in epithelial tissues[40,41]. To determine their respective roles in monolayer stress relaxation, we inhibited actin nucleation through Arp2/3 using CK666, and through formins using SMIFH2 (Supplementary Methods). Formin inhibition led to a weakly significant increase in the relaxation time τ (Fig. 3f). However, Arp2/3 inhibition had no significant effect.

To investigate the role of myosin contractility, we treated monolayers with Y27632, an inhibitor of Rho-kinase. Y27632 significantly reduced B/ε_0 (Supplementary Fig. 12f) and increased τ

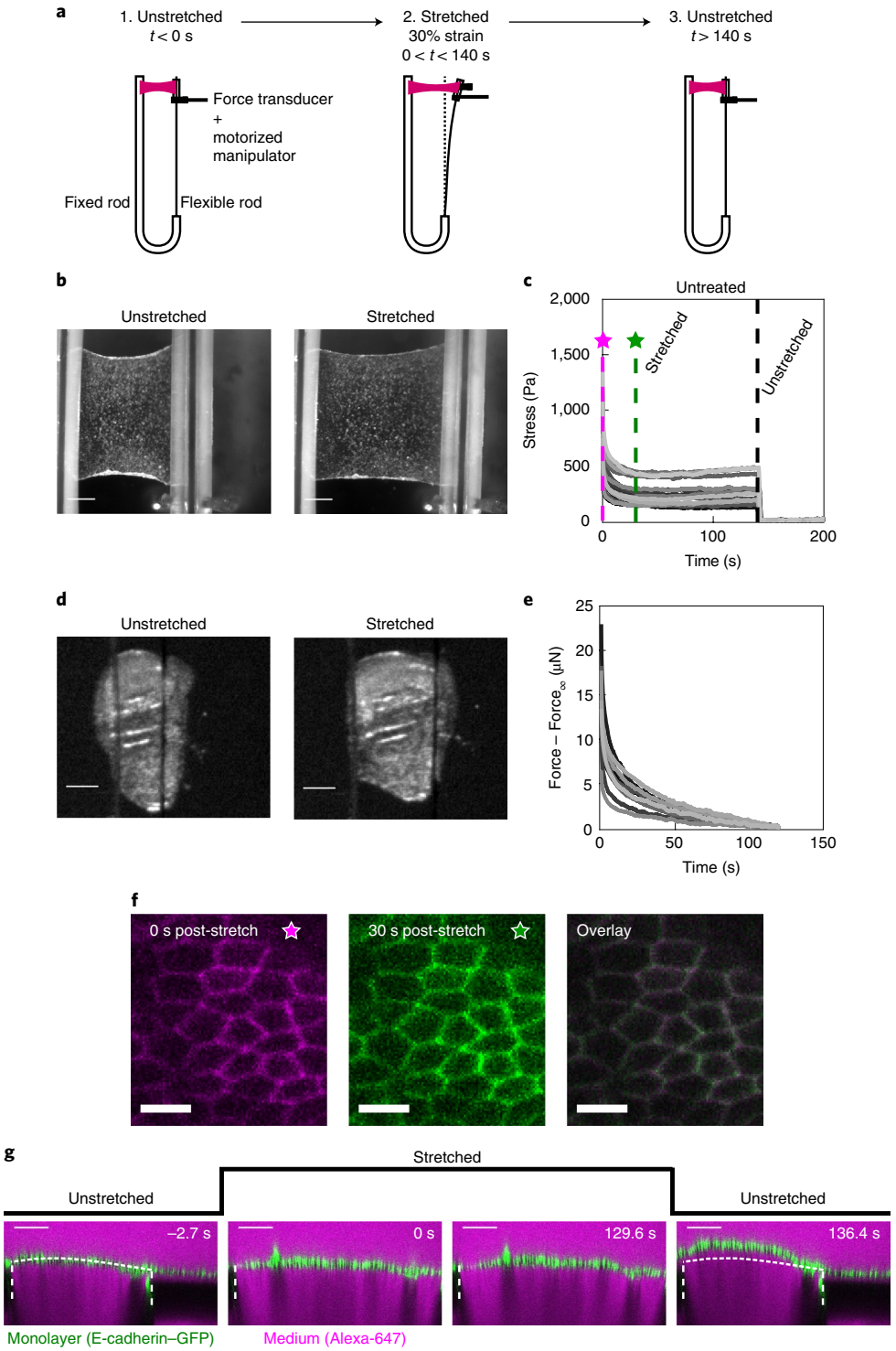

Fig. 1 | Stress relaxation in cell monolayers involves a change in length. a, Schematic diagram of the stress relaxation experiments. Monolayers were stretched to 30% strain at a 75% s^{-1} strain rate using a motorized micromanipulator and then kept at a fixed strain for about 130–140 s. The flexible rod was then returned to its initial position and the monolayers were left to recover. **b**, Bright-field microscopy images of an epithelial monolayer before and during stretch. Scale bars, 0.5 mm. **c**, Stress relaxation curves of cell monolayers ($n = 17$). The magenta and green dashed lines indicate 0 s and 30 s after application of stretch. Stresses go to zero on return of the flexible rod to its initial position ($t = 140$ s, black dashed line). **d**, Bright-field microscopy images of *Drosophila* larval wing discs before and during stretch. Scale bars, 100 μm. **e**, Stress relaxation curves of *Drosophila* larval wing discs ($n = 12$). **f**, Confocal microscopy images of monolayers expressing E-cadherin–GFP (green fluorescent protein) for 0 s (left) and 30 s (middle) after stretch. The two images were overlaid to detect potential cell shape change during relaxation (right). Scale bars, 10 μm. **g**, Cross-section of a monolayer expressing E-cadherin–GFP before application of stretch (−2.7 s), during stretch (0 s and 129.6 s) and on release (136.4 s). The length of the monolayer on release is different from its length before application of stretch. The glass substrate appears dark due to dye exclusion. The white dashed lines indicate the positions of the glass substrates. The part of the monolayer situated between the two dashed lines is suspended. The dotted white line indicates the shape of the monolayer before application of stretch. Scale bars, 100 μm. This experiment is representative of $n = 22$ monolayers.

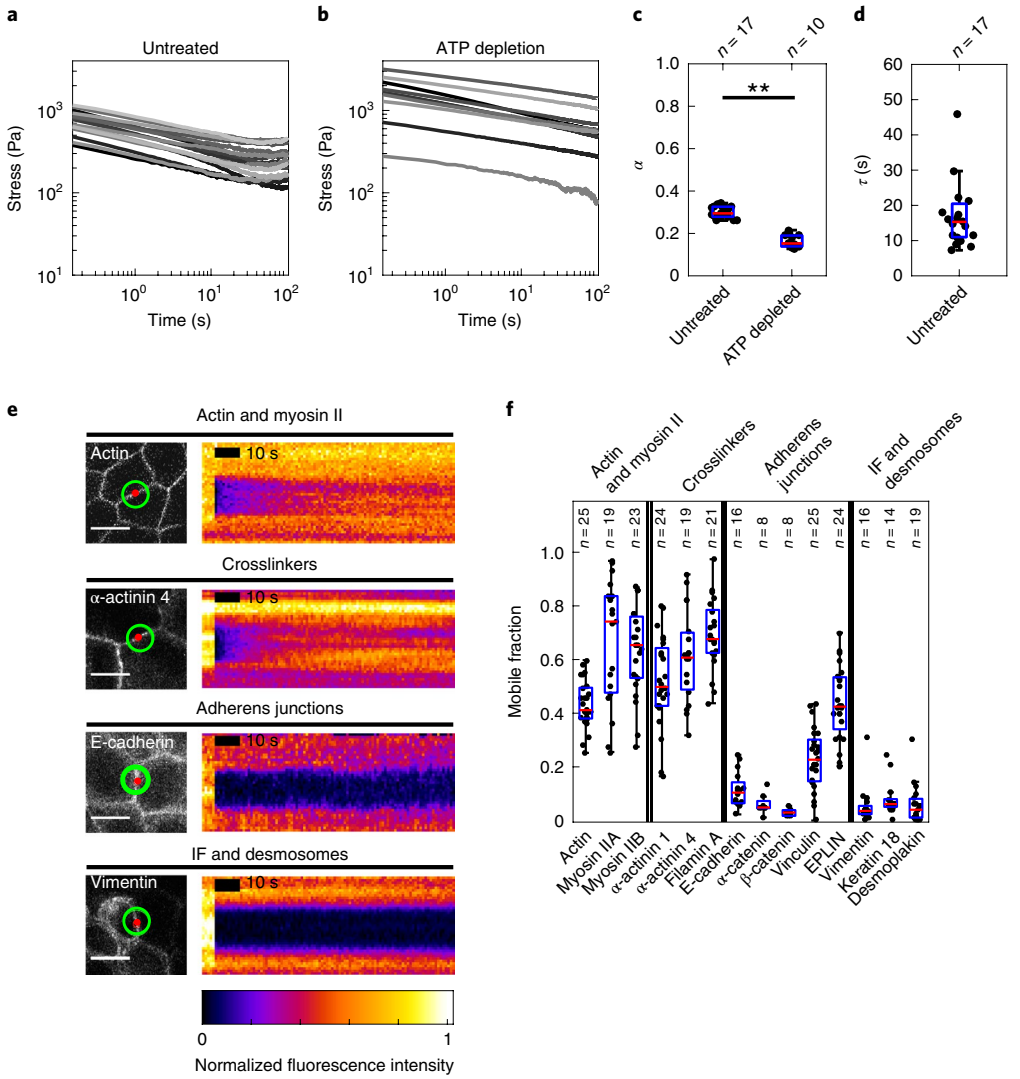

Fig. 2 | Extensive cytoskeletal remodelling occurs on the timescale of stress relaxation. a,**b**, Stress relaxation curves of untreated (**a**, $n=17$) and ATP-depleted (**b**, $n=10$) monolayers plotted on a logarithmic scale. **c**, Box plots comparing α of untreated and ATP-depleted monolayers. (** $P<0.01$.) **d**, Box plot of τ for untreated monolayers. **e**, Confocal microscopy images and kymographs of FRAP experiments. Left: localization of the protein of interest; the red circle shows the bleached region, and the green circle shows the region imaged for fluorescence recovery. Right: normalized fluorescence intensity across the junction within the green circle. Intensities are normalized to the maximum intensity in each kymograph. Scale bars, 10 μm. **f**, Mobile fractions obtained from the FRAP curves for the cytoskeletal, adhesive and junctional proteins examined. In all box plots, the number of cells or monolayers examined is indicated above the graph.

(Fig. 3f, Supplementary Fig. 12a), leading to curves that appeared more linear on a logarithmic scale and implying that myosin activity accelerates the return to mechanical equilibrium.

Finally, we explored whether crosslinkers influence the dynamics of relaxation by generating friction in the actomyosin network, as in single cells[22,42]. We found that depletion of the dominant actin crosslinkers in the system (filamin A and α-actinin 4, Supplementary Fig. 9a) had no impact on stress relaxation (Fig. 3e and Supplementary Fig. 11).

Together, these results indicate that F-actin remodelling functions together with myosin contractility to ensure rapid relaxation of stress.

Monolayer relaxation is similar to relaxation of isolated cells

Interestingly, stress relaxation in monolayers seemed similar to that in reports examining single cells[22,43]. To investigate this, we characterized the relaxation of isolated MDCK cells by compressing single rounded cells with a tipless atomic force microscopy cantilever to stretch the cortex in the free surfaces of the cell (Fig. 4a)[22]. The transitory phase of force relaxation lasts about 20 s and reports on dissipation mechanisms, while the plateau reports on cellular cortical tension[22,44] (Fig. 4b). Similarly to monolayers, single cells relaxed following a power law at second timescales and an exponential at minute timescales, consistent with previous work[22] (Fig. 4b and Supplementary Fig. 13a). Fitting these curves with our empirical function yielded $\tau=13.4\pm15.0$ s, similar to monolayers ($P=0.18$), and $\alpha=0.25\pm0.05$, weakly but significantly smaller than in monolayers ($P<0.05$, Fig. 4c,d).

Next, we investigated if the second phase of stress relaxation in single cells was sensitive to the same perturbations as in monolayers. Depletion of α-actinin 4 had no effect (Fig. 4e and Supplementary Fig. 13). Treatments with Y27632 and SMIFH2 both increased τ, as in monolayers (Fig. 4f), and decreased cellular cortical restoration force C (Supplementary Fig. 14).

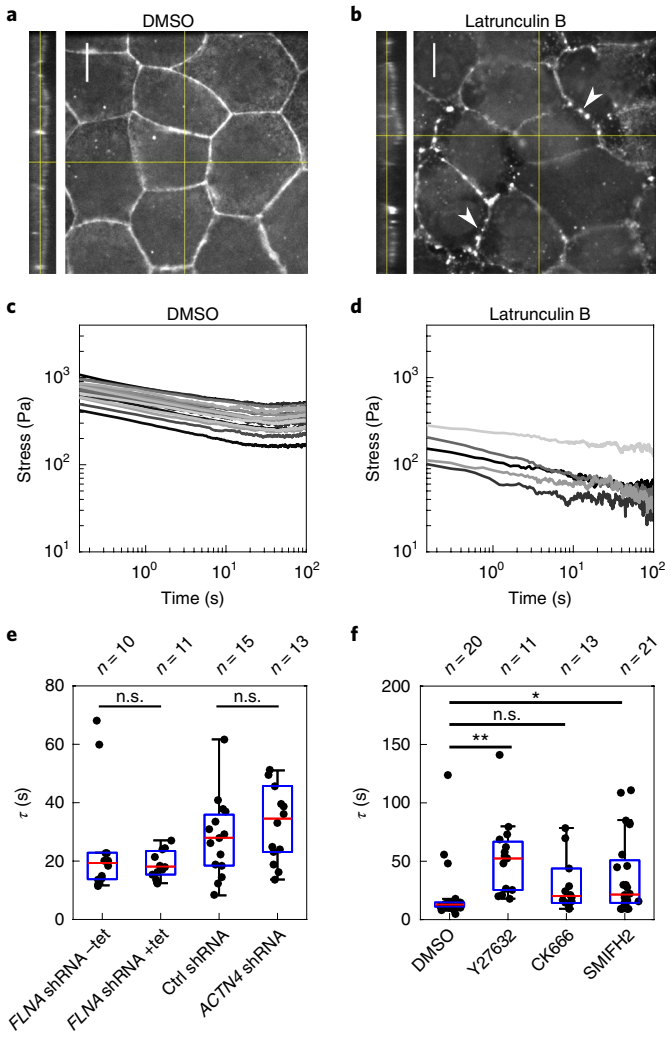

Fig. 3 | Monolayer stress relaxation is slowed by perturbations to actomyosin. a,**b**, Confocal microscopy images showing F-actin distribution in monolayers treated with dimethylsulfoxide (DMSO) (**a**) and latrunculin B (**b**) for 1 h. Junctional actin localization was perturbed following latrunculin treatment, leaving puncta of actin at the junctions (white arrowheads). Scale bars, 10 µm. The monolayer *yz* profile is shown on the left of the *xy* panel. **c**,**d**, Stress relaxation curves of monolayers treated with DMSO (**c**) and latrunculin B (**d**) for 1 h displayed on a logarithmic scale. **e**, Box plots comparing τ in monolayers depleted for actin crosslinkers filamin A and α-actinin 4 ($P = 0.34$ for *FLNA* short hairpin RNA (shRNA) + tet and $P = 0.40$ for *ACTN4* shRNA, compared with their respective controls). **f**, Box plots comparing τ following treatments with DMSO, Y27632, CK666 and SMIFH2 (**$P < 0.01$ for Y27632; n.s., $P < 0.05$ with 75% statistical power for CK666; *$P < 0.05$ for SMIFH2, all compared with DMSO). In all box plots, the number of monolayers examined is indicated above the graph.

Furthermore, we characterized actomyosin localization and turnover in single rounded cells. Actin, myosins and crosslinkers localized to the cortex of rounded cells (Supplementary Fig. 15c). Their turnover dynamics were similar to those measured in monolayers (Fig. 4g, Supplementary Fig. 15a,b and Supplementary Table 3). Therefore, single cells display similar stress relaxation to monolayers, are sensitive to similar perturbations and have similar actomyosin turnover. This suggests that stress relaxation may originate in the actin cortex, the only actin- and myosin-rich structure common to isolated cells and monolayers. Consistent with this, the mobile fraction of actin in the apical cortex of cells within monolayers was not significantly different from that in single rounded cells (0.46 ± 0.13, $P = 0.6$, Fig. 4g).

A phenomenological model for monolayer stress relaxation

To investigate the mechanical origins of the ATP-dependent regime and the dynamics of length change, we fitted the second phase of relaxation with rheological models representing the monolayer as an integrated mechanical system, in light of the similarities in the relaxation of single cells and monolayers. Based on our data, we reasoned that ATP-dependent monolayer mechanics should consist of an elastic branch, describing the response at minute-long timescales using a spring with stiffness κ, placed in parallel with a viscous branch, that describes the transitory regime (Fig. 5a, Supplementary Fig. 16a).

Although a viscous branch consisting of a spring with stiffness κ_M in series with a dashpot with viscosity η reproduces the experimental stress evolution (Supplementary Fig. 16 and Methods) and provides the evolution of monolayer length (Supplementary Methods), its characteristic time is fixed by material parameters $\tau_M = \eta/\kappa_M$ independently of strain, in contradiction with our observations (Supplementary Fig. 8g). As an alternative, we used a model that considers length as an explicit variable[45] because epithelia often change length during development[46,47]. Due to the role of myosin and changes in length during relaxation, we modelled the viscous behaviour using an active contractile element consisting of a spring with stiffness κ_A subjected to a constant prestrain ε^c (Fig. 5a). In response to an applied strain ε_0, this spring changes its resting length $L(t)$ as

$$\dot{L}/L = \gamma(\varepsilon^e(t) - \varepsilon^c)/|\varepsilon^e(t = 0\ \mathrm{s}) - \varepsilon^c|$$

with γ a length-change rate. $\varepsilon^e(t)$ is the effective strain defined as

$$\varepsilon^e(t) = (l_m - L(t))/L(t)$$

with l_m the actual length of the monolayer imposed by deformation. Over time, the change in $L(t)$ dissipates stress with an exponential decay (equation (6)), similarly to a Maxwell material (Supplementary equation (14)), converging towards the prestress $\sigma_c = \kappa_A \varepsilon^c$. After relaxation, stress in the monolayer reaches a plateau $\sigma_\infty = \kappa\varepsilon_0 + \kappa_A\varepsilon^c$ with a characteristic time that increases with strain as $\tau_{model} = \varepsilon_0/[\gamma(1 + \varepsilon_0)]$, as observed in experiments (Supplementary Fig. 8g). The resting lengths of the active branch and the elastic branch may be different because they originate from different cytoskeletal structures.

In monolayers, we measured $\sigma_c \sim 141$ Pa (Supplementary Fig. 17a,c and Supplementary Methods), consistent with an active element. Following relaxation, the stress in the elastic branch ($\sigma_\infty - \sigma_c$) seems to scale linearly with strain (Supplementary Fig. 17b), pointing to a spring-like behaviour with $\kappa \sim 1{,}006$ Pa (Supplementary Fig. 17b). We fitted the second phase of stress relaxation using equation (7) to determine κ_A and γ, using our measurements of σ_c and κ together with the relationship $\sigma_c = \kappa_A\varepsilon^c$ (Fig. 5b, Supplementary Fig. 17c–g, $\kappa_A \sim 601$ Pa, $\varepsilon^c = 0.26$ and $\gamma \sim 0.03\ \mathrm{s}^{-1}$, Methods). We then confirmed our model's robustness to variations in strain and strain rate (Supplementary Results). The τ_{model} values obtained from the model correlated well with those determined from empirical fitting for all conditions (Fig. 5f). In experiments, τ increased with applied strain (Supplementary Fig. 8d,g), a scaling that could be explicitly derived from our rheological model with no change in material parameters (Supplementary Fig. 19e and Methods). Furthermore, for small applied strain, τ_{model} becomes linearly proportional to ε_0: $\tau_{model} \sim \varepsilon_0/\gamma$. Using this approximation, linear fits of our observations (Supplementary Fig. 8g) suggest that $\tau(\varepsilon_0)$ intercepts the y axis close to 0 s (intercept $= -5.5 \pm 11.4$ s, $P = 0.31$ compared with zero), consistent with our model. The slopes of these fits predict

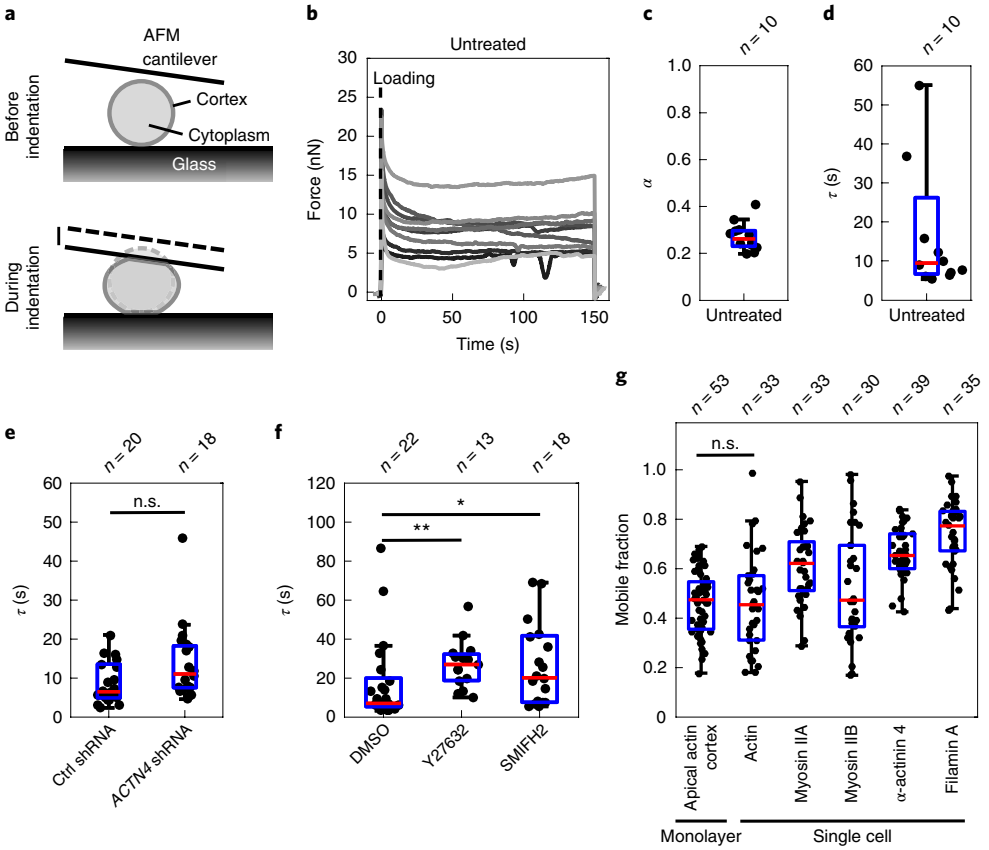

Fig. 4 | The dynamics of stress relaxation and the extent of actomyosin turnover are similar in single cells and in monolayers. a, Diagram representing the experimental setup. At time $t = 0$ s, a single rounded cell is compressed between the glass surface and a tipless atomic force microscopy cantilever. Cell compression leads to stretching of the cortex at the cell free boundaries. The evolution of force over time is measured by monitoring changes in cantilever deflection with an optical lever. **b**, Temporal evolution of force in untreated single rounded cells. A step deformation representing about 30% of cell height was applied at $t = 0$ s and maintained constant for 150 s. Each individual trace corresponds to a different cell. **c**,**d**, Box plots reporting α (**c**) and τ (**d**) for untreated rounded cells. **e**, Box plots comparing the characteristic relaxation times for cells expressing non-silencing shRNA (Ctrl shRNA) and shRNA targeting α-actinin 4 (*ACTN4* shRNA) (n.s., $P < 0.05$ with 51% statistical power). **f**, Box plots comparing the characteristic relaxation times for cells treated with DMSO, Y27632 and SMIFH2 (**$P < 0.01$ for Y27632 and *$P < 0.05$ for SMIFH2, both compared with DMSO). **g**, Box plots comparing the mobile fraction of actomyosin proteins in the cortex of rounded cells after 100 s recovery after photobleaching as well as actin turnover in the apical cortex of cells within monolayers. In all box plots, the number of cells examined is indicated above the graph.

$\gamma \sim 0.03 \pm 0.02\,s^{-1}$, similar to the values obtained by fitting relaxation curves for 30% strain (Supplementary Fig. 17e, $P = 0.28$). This suggests that γ stems from constitutive strain-independent biochemical reactions.

Myosins and formins accelerate length change

To link mechanical behaviour to biological mechanisms, we analysed perturbation experiments using our rheological model. The effect of F-actin depolymerization suggested that both branches of our model are actin-rich structures (Fig. 3a–d). Next, we measured changes to κ and σ_c from experiments and obtained κ_A and γ from curve fitting with the condition $\sigma_c = \kappa_A \varepsilon^c$. Treatment with either Y27632 or SMIFH2 decreased γ, but had no effect on κ_A (Fig. 5c,d). Therefore, both formins and myosin contractility contribute to stress relaxation by ensuring rapid length change. Interestingly, Rho-kinase inhibition also decreased σ_c and κ, while formin inhibition affected neither (Fig. 5e, Supplementary Fig. 20a and Supplementary Results). Thus, myosin contributes to both the active and the elastic parts of the system, perhaps through its different functions (contractility and crosslinking) or because each branch represents a distinct actomyosin structure.

Discussion

Here, we characterize stress relaxation and the molecular turnover of stress-bearing biological structures in isolated cells and epithelial monolayers. Our data paint a picture in which intercellular junctions form stable interconnections between cells, allowing the monolayer to behave like a single cell with its rheology controlled by cortical actomyosin. Together F-actin remodelling and myosin contractility endow the monolayer with solid-like mechanical properties at minute timescales, act as driving forces to reach a new mechanical steady state following extension and regulate monolayer length.

Monolayer rheology is controlled by cellular rheology. Stress relaxation in monolayers displayed many similarities to stress relaxation in single cells. This is surprising since the cytoskeletal organization of single rounded cells and cells within epithelia differ markedly.

Yet, when subjected to a step deformation, both single cells and monolayers displayed an initial phase of relaxation following a power law followed by an exponential decay reaching a plateau at minute-long timescales, consistent with previous reports[22,43]. The plateau indicates that both single cells and monolayers switch from

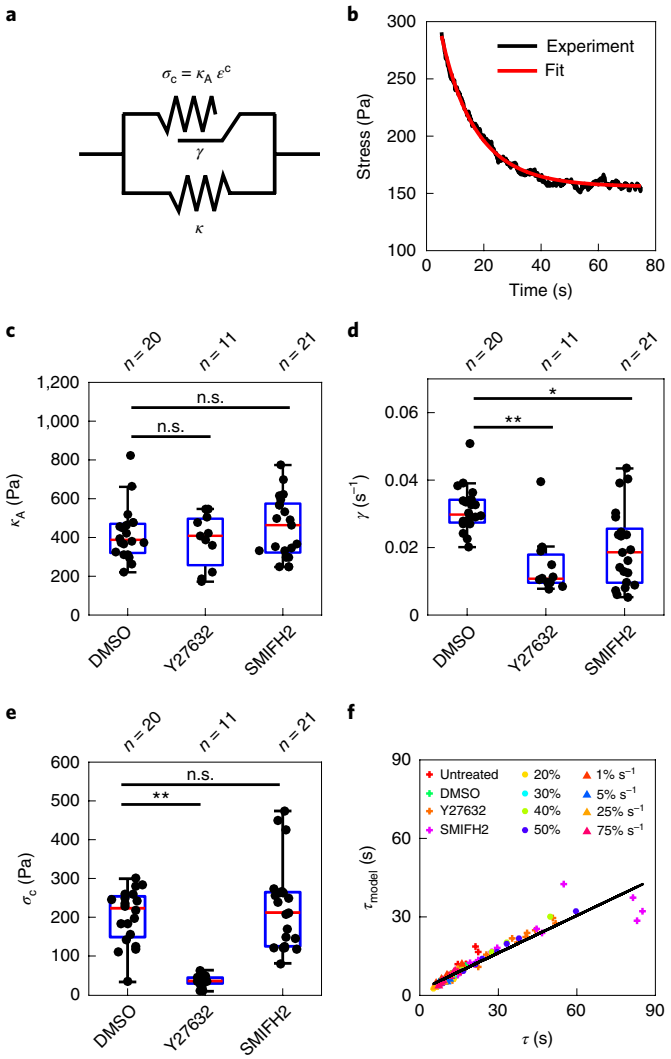

Fig. 5 | Formin-mediated actin polymerization and myosin contractility contribute to rheological properties during stress relaxation. a, Diagram of the rheological model consisting of an active branch (top) and an elastic branch (bottom). The elastic branch consists of a spring with stiffness κ and this gives the steady-state behaviour of the monolayer. The active branch describes the transitory regime in response to mechanical perturbation and it comprises an active contractile element that consists of a spring with stiffness κ_A subjected to a prestrain ε^c. This active spring can change its resting length $L(t)$ at a rate γ. **b**, The second phase of a representative relaxation curve is fitted with the rheological model shown in **a**. **c**–**e**, Box plots comparing κ_A (**c**), γ (**d**) and σ_c (**e**) for monolayers treated with DMSO, Y27632 or SMIFH2. (κ_A, n.s., $P = 0.95$ for Y27632 and $P = 0.58$ for SMIFH2; γ, $^{**}P < 0.01$ for Y27632 and $^{*}P < 0.05$ for SMIFH2; σ_c, $^{**}P < 0.01$ for Y27632 and n.s., $P = 0.80$ for SMIFH2; all compared with DMSO.) **f**, τ_{model} calculated from the rheological model using equation (9) as a function of τ determined from fitting with the empirical function (equation (1)) for the different loading regimes and the different perturbations. In all box plots, the number of monolayers examined is indicated above the graph.

a liquid-like behaviour at second timescales to a solid-like behaviour on minute-long timescales.

In the second phase of relaxation, stress in monolayers and single cells decayed with τ values that were identical (~14 s). In both situations, τ depended strongly on myosin contractility and formin activity. These similarities imply that the rheology of single cells and monolayers is governed by actomyosin structures common to both.

Molecular mechanisms controlling monolayer rheology. In line with the role of actomyosin in stress relaxation, we observed that cortical proteins turn over significantly on the timescale of mechanical relaxation in single cells and monolayers. In contrast, the adhesive structures present in monolayers remodel far less. Therefore, adherens junctions form stable interconnections between cells, allowing the monolayer to behave like a single cell with its rheology controlled by actomyosin. As the submembranous cortex is the only actomyosin-rich structure common to both single rounded cells and cells within epithelial monolayers (Supplementary Figs. 10 and 15) and as it turns over to a similar extent in both configurations (Fig. 4g), this suggests that cortical actomyosin controls stress relaxation. This further implies that rheology at the tissue scale may be controlled by emergent properties of actomyosin gels at the molecular scale[48].

Interestingly, τ increased with applied strain (Supplementary Fig. 8g), but why remodelling of the cortex should take longer for larger strain is unclear. Cortical remodelling requires nucleation of new actin filaments and depolymerization[49]. When monolayers are stretched, their apical and basal areas increase[13], potentially leading to a decrease in the concentration of actin nucleators at the membrane. As cortex thickness is regulated[50,51], the lower nucleator concentration may lead to a longer remodelling time.

Monolayer length changes in response to application of stress. Previous theoretical and experimental studies have suggested that changes in the resting length of cells and tissues may underlie stress relaxation[45,46]. In line with this, we showed that monolayer length increases in response to sustained stretch (Fig. 1g). This length change stems from a change in the length of the active branch of our model and depends on formin-mediated polymerization and myosin contractility (Fig. 5). Although length increase in the active branch dissipates part of the stress, our model and experiments indicate that the elastic branch does not change length at minute timescales. Further work will be necessary to determine which actomyosin structure underlies this elastic-like behaviour. The realization that some monolayer structures can change resting length over minute timescales in response to stress may have important consequences for our understanding of developmental morphogenesis, which often involves large tissue deformations in response to stress generated elsewhere in the embryo. Our results show that, in addition to cellular level processes,which take tens of minutes, molecular turnover can change cellular cortical area to dissipate stresses in minutes.

Online content

Any methods, additional references, Nature Research reporting summaries, source data, statements of code and data availability and associated accession codes are available at https://doi.org/10.1038/s41567-019-0516-6.

Received: 28 August 2017; Accepted: 1 April 2019;
Published online: 13 May 2019

References

1. Heisenberg, C.-P. & Bellaïche, Y. Forces in tissue morphogenesis and patterning. *Cell* **153**, 948–962 (2013).
2. Martin, A. C., Gelbart, M., Fernandez-Gonzalez, R., Kaschube, M. & Wieschaus, E. F. Integration of contractile forces during tissue invagination. *J. Cell Biol.* **188**, 735–749 (2010).
3. Tschumperlin, D. J., Boudreault, F. & Liu, F. Recent advances and new opportunities in lung mechanobiology. *J. Biomech.* **43**, 99 (2010).
4. Califano, J. P. & Reinhart-King, C. A. Exogenous and endogenous force regulation of endothelial cell behavior. *J. Biomech.* **43**, 79–86 (2010).
5. Blanchard, G. B. et al. Tissue tectonics: morphogenetic strain rates, cell shape change and intercalation. *Nat. Methods* **6**, 458–464 (2009).
6. He, Z., Ritchie, J., Grashow, J. S., Sacks, M. S. & Yoganathan, A. P. In vitro dynamic strain behavior of the mitral valve posterior leaflet. *J. Biomech. Eng.* **127**, 504–511 (2005).

7. Sacks, M. S. et al. In-vivo dynamic deformation of the mitral valve anterior leaflet. *Ann. Thorac. Surg.* **82**, 1369–1377 (2006).
8. Perlman, C. E. & Bhattacharya, J. Alveolar expansion imaged by optical sectioning microscopy. *J. Appl. Physiol.* **103**, 1037–1044 (2007).
9. Padala, M. et al. Mechanics of the mitral valve strut chordae insertion region. *J. Biomech. Eng.* **132**, 081004 (2010).
10. Maiti, R. et al. In vivo measurement of skin surface strain and sub-surface layer deformation induced by natural tissue stretching. *J. Mech. Behav. Biomed. Mater.* **62**, 556–569 (2016).
11. Korkmaz, I. & Rogg, B. A simple fluid-mechanical model for the prediction of the stress–strain relation of the male urinary bladder. *J. Biomech.* **40**, 663–668 (2007).
12. Obropta, E. W. & Newman, D. J. Skin strain fields at the shoulder joint for mechanical counter pressure space suit development. In *2016 IEEE Aerospace Conference* 2562–2570 (IEEE, 2016).
13. Harris, A. R. et al. Characterizing the mechanics of cultured cell monolayers. *Proc. Natl Acad. Sci. USA* **109**, 16449–16454 (2012).
14. Suki, B. & Hubmayr, R. Epithelial and endothelial damage induced by mechanical ventilation modes. *Curr. Opin. Crit. Care* **20**, 17–24 (2014).
15. Jufri, N. F., Mohamedali, A., Avolio, A. & Baker, M. S. Mechanical stretch: physiological and pathological implications for human vascular endothelial cells. *Vasc. Cell* **7**, 8 (2015).
16. Getsios, S., Huen, A. C. & Green, K. J. Working out the strength and flexibility of desmosomes. *Nat. Rev. Mol. Cell Biol.* **5**, 271–281 (2004).
17. Levine, E., Lee, C. H., Kintner, C. & Gumbiner, B. M. Selective disruption of E-cadherin function in early Xenopus embryos by a dominant negative mutant. *Development* **120**, 901–909 (1994).
18. Tang, V. W. & Brieher, W. M. FSGS3/CD2AP is a barbed-end capping protein that stabilizes actin and strengthens adherens junctions. *J. Cell Biol.* **203**, 815–833 (2013).
19. Wyatt, T., Baum, B. & Charras, G. A question of time: tissue adaptation to mechanical forces. *Curr. Opin. Cell Biol.* **38**, 68–73 (2016).
20. Moeendarbary, E. et al. The cytoplasm of living cells behaves as a poroelastic material. *Nat. Mater.* **12**, 253–261 (2013).
21. Trepat, X. et al. Universal physical responses to stretch in the living cell. *Nature* **447**, 592–595 (2007).
22. Fischer-Friedrich, E. et al. Rheology of the active cell cortex in mitosis. *Biophys. J.* **111**, 589–600 (2016).
23. Priya, R. et al. Feedback regulation through myosin II confers robustness on RhoA signalling at E-cadherin junctions. *Nat. Cell Biol.* **17**, 1282–1293 (2015).
24. Charras, G. & Yap, A. S. Tensile forces and mechanotransduction at cell–cell junctions. *Curr. Biol.* **28**, R445–R457 (2018).
25. Bambardekar, K., Clément, R., Blanc, O., Chardès, C. & Lenne, P.-F. Direct laser manipulation reveals the mechanics of cell contacts in vivo. *Proc. Natl Acad. Sci. USA* **112**, 1416–1421 (2015).
26. Harris, A. R. et al. Generating suspended cell monolayers for mechanobiological studies. *Nat. Protoc.* **8**, 2516–2530 (2013).
27. Roan, E. & Waters, C. M. What do we know about mechanical strain in lung alveoli? *Am. J. Physiol.—Lung Cell. Mol. Physiol.* **301**, L625–L635 (2011).
28. Wyatt, T. P. J. et al. Emergence of homeostatic epithelial packing and stress dissipation through divisions oriented along the long cell axis. *Proc. Natl Acad. Sci. USA* **112**, 5726–5731 (2015).
29. Lecuit, T. & Yap, A. S. E-cadherin junctions as active mechanical integrators in tissue dynamics. *Nat. Cell Biol.* **17**, 533–539 (2015).
30. Forgacs, G., Foty, R. A., Shafrir, Y. & Steinberg, M. S. Viscoelastic properties of living embryonic tissues: a quantitative study. *Biophys. J.* **74**, 2227–2234 (1998).
31. Kollmannsberger, P. & Fabry, B. Linear and nonlinear rheology of living cells. *Annu. Rev. Mater. Res.* **41**, 75–97 (2011).
32. Khalilgharibi, N., Fouchard, J., Recho, P., Charras, G. & Kabla, A. The dynamic mechanical properties of cellularised aggregates. *Curr. Opin. Cell Biol.* **42**, 113–120 (2016).
33. Bonnet, I. et al. Mechanical state, material properties and continuous description of an epithelial tissue. *J. R. Soc. Interface* **9**, 2614–2623 (2012).
34. Martin, A. C., Kaschube, M. & Wieschaus, E. F. Pulsed actin-myosin network contractions drive apical constriction. *Nature* **457**, 495 (2009).
35. Machado, P. F. et al. Emergent material properties of developing epithelial tissues. *BMC Biol.* **13**, 98 (2015).
36. Wang, N. & Stamenović, D. Contribution of intermediate filaments to cell stiffness, stiffening, and growth. *Am. J. Physiol.—Cell Physiol.* **279**, C188 (2000).
37. Ramms, L. et al. Keratins as the main component for the mechanical integrity of keratinocytes. *Proc. Natl Acad. Sci. USA* **110**, 18513–18518 (2013).
38. Harris, A., Daeden, A. & Charras, G. Formation of adherens junctions leads to the emergence of a tissue-level tension in epithelial monolayers. *J. Cell Sci.* **127**, 2507–2517 (2014).
39. Gonzalez-Rodriguez, D. et al. Detachment and fracture of cellular aggregates. *Soft Matter* **9**, 2282–2290 (2013).
40. Cavey, M., Rauzi, M., Lenne, P.-F. & Lecuit, T. A two-tiered mechanism for stabilization and immobilization of E-cadherin. *Nature* **453**, 751–756 (2008).
41. Kovacs, E. M. et al. N-WASP regulates the epithelial junctional actin cytoskeleton through a non-canonical post-nucleation pathway. *Nat. Cell Biol.* **13**, 934 (2011).
42. Yoshinaga, N. & Marcq, P. Contraction of cross-linked actomyosin bundles. *Phys. Biol.* **9**, 046004 (2012).
43. Desprat, N., Guiroy, A. & Asnacios, A. Microplates-based rheometer for a single living cell. *Rev. Sci. Instrum.* **77**, 055111 (2006).
44. Fischer-Friedrich, E., Hyman, A. A., Jülicher, F., Müller, D. J. & Helenius, J. Quantification of surface tension and internal pressure generated by single mitotic cells. *Sci. Rep.* **4**, 6213 (2014).
45. Muñoz, J. J. & Albo, S. Physiology-based model of cell viscoelasticity. *Phys. Rev. E* **88**, 012708 (2013).
46. Doubrovinski, K., Swan, M., Polyakov, O. & Wieschaus, E. F. Measurement of cortical elasticity in *Drosophila melanogaster* embryos using ferrofluids. *Proc. Natl Acad. Sci. USA* **114**, 1051–1056 (2017).
47. Clément, R., Dehapiot, B., Collinet, C., Lecuit, T. & Lenne, P.-F. Viscoelastic dissipation stabilizes cell shape changes during tissue morphogenesis. *Curr. Biol.* **27**, 3132–3142 (2017).
48. Prost, J., Julicher, F. & Joanny, J. F. Active gel physics. *Nat. Phys.* **11**, 111–117 (2015).
49. Salbreux, G., Charras, G. & Paluch, E. Actin cortex mechanics and cellular morphogenesis. *Trends Cell Biol.* **22**, 536–545 (2012).
50. Biro, M. et al. Cell cortex composition and homeostasis resolved by integrating proteomics and quantitative imaging. *Cytoskeleton* **70**, 741–754 (2013).
51. Chugh, P. et al. Actin cortex architecture regulates cell surface tension. *Nat. Cell Biol.* **19**, 689–697 (2017).

Acknowledgements

The authors wish to acknowledge present and past members of the Charras, Baum, Kabla and Muñoz laboratories for discussions. The authors acknowledge technical support from UCL Genomics for sequencing and analysing total RNA data as well as from J. Duque (LCN) for analysis of fluorescence intensity at junctions and from M. Vaghela (LCN) for AFM measurements. N.K. was funded by the Rosetrees Trust, the UCL Graduate School, the EPSRC funded doctoral training programme CoMPLEX and the European Research Council (ERC-CoG MolCellTissMech, agreement 647186 to G.C.). N.K. was in receipt of a UCL Overseas Research Scholarship. N.K. was supported by the Professor Rob Seymour Travel Bursary Fund for research visits to Barcelona. J.F. and A.B. were funded by BBSRC grants (BB/M003280 and BB/M002578) to G.C. and A.K. J.J.M., N.A. and P.M. acknowledge the support of the Ministry of Economy, Industry and Competitiveness through grants nos. DPI2013-43727R and DPI2016-74929-R and the Generalitat de Catalunya through grant no. 2014-SGR-1471. N.A. was also financially supported by Universitat Politècnica de Catalunya and Consorci Escola Industrial de Barcelona through grant UPC-FPI 2012, and the European Research Council under the European Community's Seventh Framework Programme (FP7/2007–2013)/ERC, grant agreement no. 240487. P.M. was also supported by the European Molecular and Biology Organization under grant ASTF 351-2016. R.B. is part of the EPSRC-funded doctoral training programme CoMPLEX. M.D. was funded by a Marie Skłodowska-Curie Horizon 2020 Individual Fellowship (MRTGS). A.Y. was supported by an HFSP Young Investigator award to G.C. (RGY 66/2013). A.H. was supported by a BBSRC grant (BB/K013521) to G.C. and A.K. Y.F. was supported by Japan Society for the Promotion of Science Grant-in-Aid for Scientific Research on Innovative Areas 26114001, Grant-in-Aid for Scientific Research (A) 18H03994, the Strategic Japanese–Swiss Science and Technology Programme, AMED under grant nos. JP17ck0106361 and JP18cm0106234, SAN-ESU GIKEN Co. Ltd, the Naito Foundation and the Takeda Science Foundation. A.K. was supported by BBSRC grants (BB/K018175/1, BB/M003280 and BB/M002578). Y.M. is funded by MRC Fellowship MR/L009056/1, a UCL Excellence Fellowship and NSFC International Young Scientist Fellowship 31650110472. B.B. is supported by UCL, a BBSRC project grant (BB/K009001/1) and a CRUK programme grant (17343). M.M. is supported by EPSRC (EP/K038656/1). G.C. is supported by a consolidator grant from the European Research Council (MolCellTissMech, agreement 647186). Atomic force microscopy equipment was purchased thanks to an ALERT16 grant from BBSRC to G.C.

Author contributions

N.K., A.H. and G.C. designed the experimental setup. N.K., A.K., B.B., M.M. and G.C. designed the experiments. N.K. carried out the relaxation experiments on monolayers and single cells. G.C. carried out FRAP experiments and protein localization experiments. A.Y. carried out western blot experiments. N.K. carried out most of the data and image analysis. J.F. designed and carried out image analysis to measure prestress. N.K. and J.F. performed length change experiments. A.B. and A.K. contributed to theoretical analysis. N.A., P.M. and J.J.M. designed the rheological model. J.J.M. contributed to computational analysis. A.K., J.J.M. and M.M. provided conceptual advice. R.B., M.D., Y.M. and N.K. carried out measurements on *Drosophila* wing disc explants. Y.F. provided cell lines. N.K., B.B. and G.C. wrote the manuscript. All authors discussed the results and the manuscript.

Competing interests

The authors declare no competing interests.

Additional information

Supplementary information is available for this paper at https://doi.org/10.1038/s41567-019-0516-6.

Correspondence and requests for materials should be addressed to G.C.

Journal peer review information: *Nature Physics* thanks Pierre-François Lenne and the other anonymous reviewer(s) for their contribution to the peer review of this work.

Methods

Cell culture and generation of cell lines. MDCK II cells were cultured at 37 °C in an atmosphere of 5% CO_2 in air in high-glucose DMEM (ThermoFisher) supplemented with 10% fetal bovine serum (Sigma) and 1% penicillin–streptomycin (ThermoFisher). Mechanical experiments and imaging were performed in Leibovitz's L15 without phenol red (ThermoFisher) supplemented with 10% fetal bovine serum.

To visualize the junctional and cytoskeletal structures, and to determine the turnover kinetics of various proteins, stable lines of MDCK II cells expressing the following proteins were used: E-cadherin–GFP, actin–GFP, Lifeact–GFP, α-catenin–GFP, β-catenin–GFP, vinculin–GFP, EPLIN–GFP, α-actinin 1–GFP, α-actinin 4–GFP, filamin A–GFP, vimentin–GFP, keratin 18–GFP, desmoplakin–GFP, NMHCIIA–GFP and NMHCIIB–GFP. Cell lines expressing E-cadherin–GFP, Lifeact–GFP and keratin 18–GFP have been described by Harris et al.[13]. Other cell lines were generated by linearization of plasmids encoding the FP-tagged protein of interest with the appropriate restriction enzyme. The following plasmids were used: α-catenin–GFP (a gift from Dr. E. Sahai, The Francis Crick Institute, UK), β-catenin–GFP (a gift from Dr. B. Henderson, University of Sydney, Australia), vinculin–GFP (a gift from Professor S. Craig, Johns Hopkins University, USA), EPLIN–GFP (a gift from Professor E. Luna, University of Massachusetts, USA, Addgene plasmid 40947), α-actinin 1–GFP[52], α-actinin 4–GFP (a gift from Professor D. Robinson, Johns Hopkins University, USA), filamin A–GFP (a gift from Dr. P. Shore, University of Manchester, UK), vimentin–GFP (a gift from Professor R. Goldman, Northwestern University, USA), desmoplakin–GFP (a gift from Professor K. Green, Northwestern University, USA, Addgene plasmid 32227), NMHCIIA–GFP and NMHCIIB–GFP (both gifts from Dr. R. Adelstein, National Heart, Lung and Blood Institute, USA, Addgene plasmids 11347 and 11348). The cell line expressing actin–GFP was generated by inserting actin–GFP into a retroviral vector (pLPCX, Takara Clontech), generating retrovirus as described by Harris et al.[13] and transducing it into MDCK cells. To create all other stable cell lines, the plasmid of interest was first linearized with the appropriate restriction enzyme and then transfected into wild-type MDCK II cells using electroporation (Lonza CLB). Approximately 10^6 cells were transfected with 10 μg (NMHCIIA–GFP, NMHCIIB–GFP) or 2 μg (all other plasmids) of plasmid DNA according to manufacturer's instructions and then selected with antibiotics for 2 weeks. To achieve a homogeneous level of fluorescence expression, cells were sorted using flow cytometry. Cells expressing E-cadherin–GFP were cultured in the presence of 250 ng ml^{-1} puromycin. Cells expressing actin–GFP were selected in the presence of 1 μg ml^{-1} puromycin. All other cell lines were selected in the presence of 1 mg ml^{-1} G418.

To study the role of crosslinkers, cell lines stably expressing shRNA targeting filamin A and α-actinin 4 were used. *FLNA* shRNA was expressed in a tetracycline-inducible manner[53]. These cells were cultured in the presence of 5 μg ml^{-1} blasticidin and 800 μg ml^{-1} G418. To induce expression of shRNA, cells were incubated in the presence of 2 μg ml^{-1} doxycycline for 72 h prior to the experiments. Plasmids encoding non-silencing shRNA and shRNA targeting α-actinin 4 were a gift from Professor B. Brieher (University of Illinois Urbana–Champaign, USA). Following linearization of the plasmids, stable cell lines expressing control shRNA and *ACTN4* shRNA were generated by transfecting the plasmids into wild-type cells using electroporation (Lonza CLB) as described above. Control and *ACTN4* shRNA lines were amplified and selected in the presence of 4 μg ml^{-1} puromycin. Protein depletion was ascertained using western blotting.

Generating suspended cell monolayers. Suspended cell monolayers were generated as described by Harris et al.[13,26]. Further information is provided in Supplementary Methods.

Mechanical testing procedure. The mechanical testing setup was assembled on top of an inverted microscope (Olympus IX-71) (Supplementary Fig. 1a). First, the Petri dish containing the stress measurement device was secured on the microscope stage with four pieces of plasticine. The force transducer (SI-KG7A, World Precision Instruments) with a tweezer-shaped mounting hook (SI-TM5-KG7A-97902, World Precision Instruments) was mounted on a three-dimensional motorized micromanipulator (Physik Instrumente) with a custom-made adaptor. The fixed rod of the device was held with the arm of a three-dimensional manual micromanipulator (Supplementary Fig. 1a), while the top Tygon section of the flexible rod was held with the tip of the force transducer (Supplementary Fig. 1c). Both motorized and manual micromanipulators were equipped with a magnetic plate that secured them to the custom-made metal stage of the microscope.

Using the motorized micromanipulator, the monolayers could be extended to different strains with controlled strain rates. Extended monolayers exerted restoring forces on the flexible rod, causing the transducer tip to bend. The extent of bending was translated into a voltage value that was converted into a digital signal using a data acquisition system (USB-1608G, Measurement Computing) and recorded onto a computer. Both the data acquisition system and the motorized micromanipulator were controlled with a custom-written code in Labview. The monolayer and the transducer tip were imaged every 0.5 s using a 2× objective (2× PLN, Olympus).

The mechanical testing procedure consisted of several steps.

- *Initial approach.* The tip of the force transducer was initially brought into contact with the Tygon tubing and then positioned such that the left tweezer arm was out of contact but within 50 μm of the Tygon tubing. This enabled identification of the contact point of the transducer tip with the device during the mechanical testing procedure (Supplementary Fig. 1c).
- *Preconditioning.* The monolayers were subjected to eight cycles of loading to a 30% target strain at a 1% s^{-1} strain rate. This ensured breakage of any residual collagen attached to the monolayer (especially close to the rods), as well as causing the samples to evolve into a 'preconditioned' state, where the slope of the stress–strain curve did not change in successive cycles. Hence, several experiments could be conducted on the same sample with a high degree of reproducibility.
- *Stress relaxation experiments.* The monolayers were extended to 30% strain at a 75% s^{-1} strain rate and then kept at a fixed 30% strain for about 130–140 s. The micromanipulator was then returned to the position it occupied before stretch (Fig. 1a). This released the monolayers and they were left unstretched for about 130–140 s to recover before performing another stress relaxation experiment. This stress relaxation experiment was repeated three times on each monolayer.
- *Loading until failure.* The monolayers were extended until failure at 1% s^{-1} strain rate. After rupturing the monolayer, the flexible rod was returned to its initial position.
- *Calibration of the device.* To allow conversion from voltages to force, the device was calibrated. To do this, the wire was extended at the same rate and to the same extent as in the cycling experiments. This was repeated five times. The length of the wire L_w was measured using a Canon FD macro lens interfaced to a Hamamatsu EMCCD camera (Orca ER) (Supplementary Fig. 1b). Together with the mechanical properties of the wire, knowledge of L_w enables determination of the bending stiffness of the wire and hence the force applied for a given deflection.

A detailed description of the procedure for conversion of voltages to forces is given in Supplementary Methods.

***Drosophila* wing disc mechanical testing.** The stress measurement devices and the mechanical testing procedure used for the *Drosophila* wing discs were similar to those for monolayers with a few modifications (see Supplementary Methods).

Single-rounded-cell mechanical testing procedure. Prior to experiments, MDCK cells were trypsinized and plated sparsely in a glass-bottomed Petri dish (35 mm diameter, WPI) and left to settle for 10–30 min. The experiments were conducted while the cells remained rounded and before they started to spread.

Force relaxation measurements were conducted using a CellHesion 200 atomic force microscope (JPK Instruments) mounted on a scanning laser confocal microscope (Olympus IX81 with a FV1000 confocal head) and tipless silicon SPM-sensor cantilevers (Arrow TL1Au-50, NanoWorld) with nominal spring constant of 0.03 N m^{-1} were used. The sensitivity of each cantilever was measured from the slope of a force–displacement curve acquired on a glass coverslip, and the spring constant was calibrated using the thermal noise fluctuation method. The spring constants estimated for each experiment ranged between 0.055 and 0.06 N m^{-1}.

Before conducting force relaxation experiments, force–displacement curves were acquired on the cell and a glass region close to it. Using these two curves, we estimated the cell height as the difference between the cantilever contact with the cell and glass. Next, we estimated the target force required to indent the cell by about 30%. Finally, force relaxation curves were acquired by indenting the cell to the target force of 5–40 nN at a rate of 75% s^{-1} and maintaining the cantilever at a constant height for 150 s while the force was recorded.

Analysis of the relaxation curves. To analyse the response of monolayers to a step deformation, the first 75 s of the stress relaxation curves was fitted with a function consisting of a power law with an exponential cut-off:

$$\sigma(t) = At^{-\alpha} e^{-\frac{t}{\tau}} + B \quad (1)$$

The fitting procedure was as follows. First, the initial conditions for the fitting were determined. B was the residual stress after the curves plateaued and was defined as the average of stress in the range $70\,\mathrm{s} < t < 75\,\mathrm{s}$. $A + B$ was defined as the initial stress at the second time point ($t = 0.150$ s) after the step deformation (Supplementary Fig. 3a). The first time point after application of the step deformation was ignored to allow the calculations to be performed on a logarithmic scale. To estimate α, the first 5 s of the curves was used. In practice, $\sigma(t < 5\,\mathrm{s}) - B$ was plotted as a function of time on a logarithmic scale and fitted with a line, with α being the slope of this line (Supplementary Fig. 3b). To estimate τ, $\sigma(5\,\mathrm{s} < t < 20\,\mathrm{s}) - B$ was plotted on a semilogarithmic scale and fitted with a line, with τ being the slope of this line (Supplementary Fig. 3c). Each experimental relaxation curve was fitted using equation (1), with the free parameters A, α and τ. B was also allowed to vary by 15% to optimize the fits (Supplementary Fig. 3d). The trust-region-reflective least-squares algorithm, a built-in MATLAB fitting procedure, was used for the fitting. The fitting was performed for the three individual repeats of the stress relaxation experiments on each monolayer. The fitted values obtained from the three repeats were then averaged to obtain a single value for each parameter.

For ATP-depletion experiments, we followed the same general procedure except that we fitted experimental curves with a function of the form $At^{-\alpha}$.

The same procedures were also followed to fit the relaxation curves of single rounded cells and larval wing discs. For single-cell relaxation curves, since the residual force reports on cortical restoration force, we have denoted it by a different parameter C, which was estimated and fitted similarly to B for monolayers. Due to the slower relaxation of the larval wing discs, we fitted the first 120 s of the relaxation curves and B was defined as the average of stress in the range $115\,\mathrm{s} < t < 120\,\mathrm{s}$.

The goodness of fit was determined using the coefficient of determination r^2, and curves with $r^2 < 0.80$ were excluded from further analysis. This represented fewer than 3% of experimental curves acquired. We also ensured that there was no systematic bias in the fit residuals. Outliers were determined as described in the statistical analysis section, and the curves for which either of the two parameters α and τ were outliers were not included for statistical analysis. On average, fewer than 13% of the data were excluded from analysis.

Analysis of the relaxation curves taking loading into account. The relaxation modulus $G(t)$ describes the behaviour of a viscoelastic material and is obtained from the response of the material to a step in strain. This ideal loading condition cannot be achieved experimentally. In practice, strain is applied with a constant strain rate $\dot{\varepsilon}$ until the target strain ε_0 is reached, after which strain is kept constant. Thus, the temporal evolution of stress $\sigma(t)$ in the material is given by the convolution between the relaxation modulus and the derivative of the strain:

$$\sigma(t) = \int_0^t G(t-t')\frac{\mathrm{d}\varepsilon(t')}{\mathrm{d}t'}\mathrm{d}t' \tag{2}$$

where the relaxation modulus is of the form $G(t) = A' t^{-\alpha} \mathrm{e}^{-\frac{t}{\tau}} + B'$ and A' and B' are related to A and B in equation (1) as follows: $A = \varepsilon_0 A'$ and $B = \varepsilon_0 B'$.

We fitted the relaxation responses of monolayers loaded at a $75\%\,\mathrm{s}^{-1}$ strain rate, using equation (2). Due to the singularity of $G(t)$ at $t = 0$ s, we fitted the relaxation curves in the range $[\Delta t, t_{\max}]$, with Δt being 0.150 s (our experimental timestep). The response of the material predicted using the average parameters extracted from fitting with equation (2) (Supplementary Fig. 7a, black line) are in good agreement with those obtained approximating our experimental conditions to an ideal step strain (Supplementary Fig. 7a, red line). Statistical comparisons indicate that the parameters obtained through both methods are not significantly different (Supplementary Table 2). Thus, the relaxation responses obtained for strain rates of $75\%\,\mathrm{s}^{-1}$ can be approximated by an ideal step strain.

Chemical treatments. Chemical treatments are described in detail in Supplementary Methods.

Fitting the second phase of the relaxation with the standard linear solid model. The second phase of the relaxation curves (defined for $t > 6$ s) was fitted with the standard linear solid model, which consists of an elastic branch with stiffness κ in parallel with a Maxwell branch (Supplementary Fig. 16a). The Maxwell branch consists of a spring of stiffness κ_M in series with a dashpot of viscosity η.

Following application of a step strain ε_0 at $t = 0$ s, the stress in the Maxwell branch will relax as follows:

$$\sigma_M(t) = \varepsilon_0 \kappa_M \, \mathrm{e}^{-\frac{\kappa_M}{\eta}t} \tag{3}$$

The characteristic time for this relaxation is

$$\tau_M = \frac{\eta}{\kappa_M} \tag{4}$$

Experimental data $\sigma_{raw}(t)$ were fitted as follows. First, the residual stress B was subtracted from the raw stress because it represents the stress in the elastic branch and stays constant over time. Next, the stress in the Maxwell branch (that is $\sigma_M(t) = \sigma_{raw}(t) - B$) was fitted with the stress relaxation function (3), allowing κ_M and η to vary. 88% of the fitted curves had $r^2 > 0.8$.

Fitting the second phase of the relaxation with the rheological model. The second phase of the relaxation curves (defined for $t > 6$ s) was fitted with the rheological model shown in Fig. 5a, which consists of an elastic branch with stiffness κ and an active branch. The active branch consists of a spring of stiffness κ_A subjected to a prestrain ε^c that can adapt its resting length $L(t)$ to return to ε^c after extension. Thus, in response to an ε_0 that changes l_m from l_0 to l_1, the monolayer stress is $\sigma(t) = \kappa\varepsilon_0 + \kappa_A \varepsilon^e(t)$ with $\varepsilon^e(t) = \frac{l_m - L(t)}{L(t)}$.

In our modelling, we used the following evolution law for the $L(t)$ of the active branch:

$$\frac{\dot{L}}{L} = \gamma \frac{(\varepsilon^e(t) - \varepsilon^c)}{|\varepsilon^e(0) - \varepsilon^c|} \tag{5}$$

In choosing our empirical evolution function, we reasoned that the material parameters describing the response of the active element, γ, ε^c and κ_A, should not change when we fit experimental curves for different applied strains because the initial state of the monolayer is the same (Supplementary Figs. 8 and 19).

Following application of a step strain at $t = 0$ s that changes the actual length from $l_m = l_0$ to $l_m = l_1$, the resting length $L(t)$ will adapt. Since the monolayers are prestressed and contractile, the value of the resting length before application of the deformation is given by $L(0^-) = l_0/(1+\varepsilon^c)$. This provides the initial prestrain: $\varepsilon^c = [l_0 - L(0^-)]/L(0^-)$. Using equation (5), the evolution of the resting length is calculated as

$$L(t) = \frac{l_0}{1+\varepsilon^c}\left[(1+\varepsilon_0) - \varepsilon_0 \, \mathrm{e}^{-\frac{\gamma}{\varepsilon_0}t}\right] \tag{6}$$

Knowing that $\sigma = \kappa_A \varepsilon^e$, this will lead to stress relaxation in the active branch after application of deformation of the form

$$\sigma_A(t) = \kappa_A \left(\frac{(1+\varepsilon_0)(1+\varepsilon^c)}{(1+\varepsilon_0) - \varepsilon_0 \, \mathrm{e}^{-\frac{\gamma}{\varepsilon_0}t}} - 1 \right) \tag{7}$$

where ε_0 is defined as $\varepsilon_0 = \frac{l_1 - l_0}{l_0}$.

The τ_{model} for this relaxation can be calculated as

$$\tau_{model} = \left(\frac{\mathrm{d}\sigma}{\mathrm{d}t}\bigg|_{t=0} \right)^{-1} (\sigma(\infty) - \sigma(0)) \tag{8}$$

$$\tau_{model} = \frac{\varepsilon_0}{\gamma(1+\varepsilon_0)} \tag{9}$$

Experimental data $\sigma_{raw}(t)$ were fitted as follows. First, the residual stress B was subtracted from the raw stress because it represents the stress in the elastic branch and stays constant over time. σ_c was determined in separate measurements because it cannot be determined during stress relaxation experiments (Supplementary Methods and Supplementary Fig. 17a,c). This prestress was then added to the stress in the active branch to yield $\sigma_A(t) = \sigma_{raw}(t) - B + \sigma_c$. Knowing that the measured σ_c is equal to $\kappa_A \varepsilon^c$, we substituted ε^c with σ_c/κ_A in equation (7) and $\sigma_A(t)$ was fitted with the stress relaxation function (7), allowing κ_A and γ to vary. The obtained analytical curves fitted the experimental data well ($r^2 > 0.8$ for 88% of the relaxation curves) without any systematic bias in the residuals.

Statistical analysis. All data analysis and curve fitting were conducted using custom-written code in MATLAB. For each dataset, outliers were defined as the values that fell outside the range $[q_1 - w(q_3 - q_1), q_3 + w(q_3 - q_1)]$, where q_1 and q_3 were the 25th and 75th percentiles of the data and w was 1.5. Outliers were excluded from statistical analysis. The normality of the data was tested using both Lilliefors and Shapiro–Wilk tests in R, which confirmed the non-normality of some datasets. Statistical analysis was performed in MATLAB, using a two-sided Wilcoxon rank sum test that does not assume normality of the data. To determine whether a single dataset was significantly different from zero, a Wilcoxon signed rank test in MATLAB was used. Datasets with $P < 0.01$ were deemed to be highly significantly different and are denoted by a double asterisk (**). Datasets with $P < 0.05$ were deemed to be significantly different and are denoted by a single asterisk (*). Changes with $P > 0.05$ or where statistical power was less than 0.8 were considered non-significant. For all box plots, the edges of the box represent the 25th and 75th percentiles of the data, the red line marks the median and the whiskers extend to include the most extreme data points that are not considered to be outliers. Points on each box plot represent individual monolayers or cells. Each dataset is pooled across experiments performed on at least three separate days.

Reporting Summary. Further information on research design is available in the Nature Research Reporting Summary linked to this article.

Data availability

All data supporting the conclusions are available from the authors on reasonable request.

Code availability

Custom-written code used for data analysis is available from the authors on request.

References

52. Charras, G. T., Hu, C. K., Coughlin, M. & Mitchison, T. J. Reassembly of contractile actin cortex in cell blebs. *J. Cell Biol.* **175**, 477–490 (2006).
53. Kajita, M. et al. Filamin acts as a key regulator in epithelial defence against transformed cells. *Nat. Commun.* **5**, 4428 (2014).

nature research

Corresponding author(s): Guillaume Charras

Last updated by author(s): Mar 21, 2019

Reporting Summary

Nature Research wishes to improve the reproducibility of the work that we publish. This form provides structure for consistency and transparency in reporting. For further information on Nature Research policies, see Authors & Referees and the Editorial Policy Checklist.

Statistics

For all statistical analyses, confirm that the following items are present in the figure legend, table legend, main text, or Methods section.

n/a	Confirmed	
☐	☒	The exact sample size (*n*) for each experimental group/condition, given as a discrete number and unit of measurement
☐	☒	A statement on whether measurements were taken from distinct samples or whether the same sample was measured repeatedly
☐	☒	The statistical test(s) used AND whether they are one- or two-sided *Only common tests should be described solely by name; describe more complex techniques in the Methods section.*
☒	☐	A description of all covariates tested
☐	☒	A description of any assumptions or corrections, such as tests of normality and adjustment for multiple comparisons
☐	☒	A full description of the statistical parameters including central tendency (e.g. means) or other basic estimates (e.g. regression coefficient) AND variation (e.g. standard deviation) or associated estimates of uncertainty (e.g. confidence intervals)
☐	☒	For null hypothesis testing, the test statistic (e.g. *F*, *t*, *r*) with confidence intervals, effect sizes, degrees of freedom and *P* value noted *Give P values as exact values whenever suitable.*
☒	☐	For Bayesian analysis, information on the choice of priors and Markov chain Monte Carlo settings
☒	☐	For hierarchical and complex designs, identification of the appropriate level for tests and full reporting of outcomes
☒	☐	Estimates of effect sizes (e.g. Cohen's *d*, Pearson's *r*), indicating how they were calculated

Our web collection on statistics for biologists contains articles on many of the points above.

Software and code

Policy information about availability of computer code

Data collection	- Confocal microscopy images were acquired using Olympus FV 10 ASW software, or Andor iQ1 and IQ3. - AFM data were acquired using JPK SPM Desktop. - Force measurements were acquired using Labview Virtual Instruments (VI) provided with the data acquisition system (USB-1608G, Measurement Computing) and the motorised stage (MG126.DG1 motorised stage with Mercury DC motor controller, Physik Instrumente).
Data analysis	- Confocal microscopy images of the cell monolayers were segmented using PackingAnalyzer (Aigouy et al. Cell. 2010). - For RNASeq data analysis, the following softwares were used: Illumina's bcl2fastq Conversion Software v2.16, Tophat 2.014, Picard Tools 1.79, HTSeq, BioConductor package DESeq2. - Statistical power was calculated using G*Power (Faul et al. Bahavior Research Methods. 2007). - Normality tests were conducted in R. - Microscopy images were processed in ImageJ. Alignment of the images were performed using the ImageJ plugin "Template Matching and Slice Alignment" (Tseng, Q. et al. Lab on a Chip 11, 2231-2240, 2011). - All other analysis was conducted using custom-written code in Matlab R2015b.

For manuscripts utilizing custom algorithms or software that are central to the research but not yet described in published literature, software must be made available to editors/reviewers. We strongly encourage code deposition in a community repository (e.g. GitHub). See the Nature Research guidelines for submitting code & software for further information.

Data

Policy information about availability of data

All manuscripts must include a data availability statement. This statement should provide the following information, where applicable:

- Accession codes, unique identifiers, or web links for publicly available datasets
- A list of figures that have associated raw data
- A description of any restrictions on data availability

All data supporting the conclusions are available from the authors on reasonable request.

Field-specific reporting

Please select the one below that is the best fit for your research. If you are not sure, read the appropriate sections before making your selection.

☒ Life sciences ☐ Behavioural & social sciences ☐ Ecological, evolutionary & environmental sciences

For a reference copy of the document with all sections, see nature.com/documents/nr-reporting-summary-flat.pdf

Life sciences study design

All studies must disclose on these points even when the disclosure is negative.

Sample size	Based on preliminary observations for untreated monolayers, we estimated the required sample size that allowed detection of a minimum of 50% change in the rate of the second phase of the relaxation (i.e. time constant) using G*Power, an open-source software for statistical power calculations (Faul et al. Behavior Research Methods. 2007). With the preliminary estimate of the time constant (11.5 s) and assuming the same variance for all conditions (~4s), the sample size required to detect a minimum of 50% change at the level of 0.01 significance with 80% power was n=14. In conditions where equal number of samples was not possible, we estimated that n1=19 for control conditions and n2=11 for perturbation conditions would give the same statistical power. After performing the experiments, the observed statistical power (i.e. post-hoc power) was also calculated.
Data exclusions	Where analysis involved curve fitting, goodness of fit was determined using the coefficient of determination, R-squared, and curves with R-squared<0.8 were excluded from statistical analysis. In addition, for each dataset, outliers were defined as the values that fell outside the range [q1-w(q3-q1),q3+w(q3-q1)], where q1 and q3 were the 25th and 75th percentiles of the data and w was 1.5. Outliers were excluded from statistical analysis. The reported n numbers in the manuscript are the number of data points included in the statistical analysis after data exclusion.
Replication	All replicates reported in the manuscript are biological replicates collected from experiments performed on at least 3 individual days.
Randomization	On each day of experiment, care was taken to perform control and perturbation conditions in a randomised order.
Blinding	NA

Reporting for specific materials, systems and methods

We require information from authors about some types of materials, experimental systems and methods used in many studies. Here, indicate whether each material, system or method listed is relevant to your study. If you are not sure if a list item applies to your research, read the appropriate section before selecting a response.

Materials & experimental systems

n/a	Involved in the study
☐	☒ Antibodies
☐	☒ Eukaryotic cell lines
☒	☐ Palaeontology
☐	☒ Animals and other organisms
☒	☐ Human research participants
☒	☐ Clinical data

Methods

n/a	Involved in the study
☒	☐ ChIP-seq
☒	☐ Flow cytometry
☒	☐ MRI-based neuroimaging

Antibodies

Antibodies used	- Mouse anti-filamin A monoclonal (Sigma, cat. no. F6682, clone PM6/317). - Rabbit anti-alpha-actinin 4 monoclonal (Merck Millipore, cat. no. MABT144, clone EPR2533(2)). - Mouse anti-GAPDH monoclonal (Novus Biologicals, cat. no. NB300-221, clone 1D4).

- Sheep anti-mouse HRP (GE Healthcare, cat. no. NXA931)
- Donkey anti-rabbit HRP (GE Healthcare, cat. no. NA934VS)

Validation

- Mouse anti-filamin A monoclonal (Sigma, cat. no. F6682, clone PM6/317). According to manufacturer's website, "species recognition includes monkey, hamster, bovine, and canine filamin. The antibody may be used in several immunological techniques including immunoblotting and immunofluorescence". The antibody has been previously used for immunoblotting in MDCK cells (Kajita et al. Nat. Commun. 2014). We also tested the reactivity with MDCK cells by running control immunoblots.
- Rabbit anti-alpha-actinin 4 monoclonal (Merck Millipore, cat. no. MABT144, clone EPR2533(2)). According to manufacturer's website, the antibody "is validated for use in WB, IC, IH(P), IP for the detection of Alpha-Actinin 4" and reacts with human, mouse and rat Alpha-Actinin 4. We tested the reactivity with MDCK cells by running control immunoblots.
- Mouse anti-GAPDH monoclonal (Novus Biologicals, cat. no. NB300-221, clone 1D4). According to manufacturer's website, the antibody can be used in several immunological techniques including western blotting. The manufacturer has not tested reactivity with canine but states that the antibody is likely to react with other mammals. We tested reactivity by running control immunoblots and verifying that the weigh of the protein was correct.

Eukaryotic cell lines

Policy information about cell lines

Cell line source(s)	MDCK II cells were obtained from Prof. Yasuyuki Fujita.
Authentication	NA
Mycoplasma contamination	All cell lines were tested negative for mycoplasma contamination. Tests were conducted using MycoAlert PLUS detection kit (Lonza, cat. no. LT07-710).
Commonly misidentified lines (See ICLAC register)	No commonly misidentified cell lines were used.

Animals and other organisms

Policy information about studies involving animals; ARRIVE guidelines recommended for reporting animal research

Laboratory animals	Wing disc explants from wild type (yw;;) Drosophila 3rd instar larvae were used.
Wild animals	NA
Field-collected samples	NA
Ethics oversight	No ethical approval or guidance was required, as Drosophila is not protected under the Animals Scientific Procedures Act 1986.

Note that full information on the approval of the study protocol must also be provided in the manuscript.